CHEMISTRY OF MATERIALS
Article

Chem. Mater. **2010,** *22,* 5845–5855 5845
DOI:10.1021/cm101698b

Overpotential-Dependent Phase Transformation Pathways in Lithium Iron Phosphate Battery Electrodes

Yu-Hua Kao,[†] Ming Tang,[‡] Nonglak Meethong,[§] Jianming Bai,[∥] W. Craig Carter,[†] and Yet-Ming Chiang*[,†]

[†]*Massachusetts Institute of Technology, 77 Massachusetts Avenue, Building 13, Room 13-4086, Cambridge, Massachusetts 02139, United States,* [‡]*Lawrence Livermore National Laboratory, Livermore, California 94550, United States,* [§]*Khon Kaen University, Muang District, Khon Kaen, Thailand, and* [∥]*Oak Ridge National Laboratory, Oak Ridge, Tennessee 37831, United States*

Received June 18, 2010. Revised Manuscript Received September 5, 2010

An objective in battery development for higher storage energy density is the design of compounds that can accommodate maximum changes in ion concentration over useful electrochemical windows. Not surprisingly, many storage compounds undergo phase transitions *in situ*, including production of metastable phases. Unique to this environment is the frequent application of electrical over- and underpotentials, which are the electrical analogs to undercooling and superheating. Surprisingly, overpotential effects on phase stability and transformation mechanisms have not been studied in detail. Here we use synchrotron X-ray diffraction performed in situ during potentiostatic and galvanostatic cycling, combined with phase-field modeling, to reveal a remarkable dependence of phase transition pathway on overpotential in the model olivine $Li_{1-x}FePO_4$. For a sample of particle size ~113 nm, at both low (e.g., <20 mV) and high (>75 mV) overpotentials a crystal-to-crystal olivine transformation dominates, whereas at intermediate overpotentials a crystalline-to-amorphous phase transition is preferred. As particle sizes decrease to the nanoscale, amorphization is further emphasized. Implications for battery use and design are considered.

Introduction

Material properties such as crystallite size, shape, and composition, and external variables such as temperature and pressure, affect phase stability and formation in all systems. In electrochemical systems, an important additional environmental variable is the electrical under- or overpotential, which may produce very large Nernstian driving forces without the usual coupling between thermodynamic driving force and kinetics that occurs in phase transitions due to temperature. [The overpotential is here defined as the magnitude by which the potential exceeds the material's equilibrium Nernst potential; the term "overpotential" describes both the overpotential during charging and the underpotential during discharging.] Instead, the magnitude of driving force may be widely varied with only weak coupling to (temperature-dependent) kinetics; metastable phases may often be produced under conditions far from equilibrium. One example is the amorphization (i.e., glass) transition that has recently been observed to occur isothermally during electrochemical cycling of several storage compounds used in rechargeable lithium batteries, including silicon,[1,2] LiMPO$_4$ olivines,[3,4] and Li_2FeSiO_4.[5]

For detailed investigation of the relationship between electrochemical driving force and phase transformation pathways, we selected a technologically relevant model material, olivine $Li_{1-x}FePO_4$, representative of the broader class LiMPO$_4$ (M = Fe, Mn, Co, Ni). These compounds have been characterized with a classical first-order phase transition between lithiated and delithiated olivine phases.[6,7] However, a competing amorphization transition intrudes as crystallite sizes decrease to about 100 nm.[3] The particle-size dependence is consistent with a continuum thermodynamic model[4] which predicts that amorphous phase can form preferentially from olivine upon delithiation. There is a critical size for amorphization that depends on volume and interfacial energy contributions and the misfit strain between the equilibrium crystalline phases.

Additionally, the phase transition pathways should be overpotential-dependent: amorphization is expected for overpotentials above a critical value of tens of millivolts. There are significant consequences of overpotential-dependent phase transition behavior. For example, in applications such as hybrid or all-electric vehicle batteries, charge/discharge

*Corresponding author phone: (617)253-6471; fax: (617)253-6201; e-mail: ychiang@mit.edu.

(1) Limthongkul, P.; Jang, Y.-I.; Dudney, N. J.; Chiang, Y.-M. *Acta Mater.* **2003**, *51*, 1103.
(2) Obrovac, M. N.; Christensen, L. *Solid State Lett.* **2004**, *7*, A93.
(3) Meethong, N.; Kao, Y.-H.; Tang, M.; Huang, H.-Y.; Carter., W. C.; Chiang, Y.-M. *Chem. Mater.* **2008**, *20*, 6189.
(4) Tang, M.; Huang, H.-Y.; Meethong, N.; Kao, Y.-H.; Carter, W. C.; Chiang, Y.-M. *Chem. Mater.* **2009**, *21*, 1557.
(5) Dominko, R *J. Power Sources* **2008**, *184*, 462.
(6) Padhi, A. K.; Najundaswamy, K. S.; Goodenough, J. B. *J. Electrochem. Soc.* **1997**, *144*, 1188.
(7) Andersson, A. S.; Kalska, B.; Häggström, L; Thomas, J. O. *Solid State Ionics* **2000**, *130*, 41.

Published on Web 10/14/2010

protocols produce frequent voltage transients and thus overpotentials; these may produce unexpected and history-dependent phase states. Phase-state hysteresis in storage electrodes may depend on instantaneous operating conditions as well as the material's usage history. This has direct consequences on *in situ* monitoring of state-of-charge (SOC), impedance, storage kinetics, and battery durability due to electrochemical-mechanical coupling.[8] Predictions of overpotential- and time-dependent phenomena could also permit phase states and transition pathways to be electrochemically controlled.

Experimental Section

To measure overpotential dependence, lithium half-cells were potentiostatically and galvanostatically cycled while diffraction data were obtained *in situ*. These tests were performed on two reference (undoped) $Li_{1-x}FePO_4$ powders for which extensive data have previously been obtained.[3,9−11] The starting powders were prepared as composite electrode coatings on aluminum foil current collectors and assembled in modified lithium half-cells. Powder diffraction spectra were collected in transmission mode using a linear position-sensitive silicon detector.

Samples and *In Situ* Cell Design. Powder sample A is a commercially sourced "carbon-added" $LiFePO_4$ (Aldrich Chemical) having 14.8 m^2/g BET specific surface area and 113 nm equivalent spherical particle diameter. Sample B was synthesized as described in ref 12 and has a BET specific surface area of 48.8 m^2/g, corresponding to an equivalent spherical particle diameter of 34 nm. This sample was also examined after heat-treating at 800 °C for 5 h in argon atmosphere to coarsen it to 7.6 m^2/g and 220 nm equivalent spherical particle diameter. Electrodes were fabricated by mixing 79 wt % positive active material, 10 wt % conductive carbon black (Super P, MMM Carbon, Brussels, Belgium), and 11 wt % Kynar 2801 binder, and acetone as a solvent. The formulation was coated onto 25 μm thick aluminum foil current collectors at loadings of ~3.5 and 7 mg/cm^2 of active material for final coating thickness of ~150 and 225 μm, respectively. The in situ transmission cells used modified coin-cell hardware (CR-2025). A small circular window (0.25 in. diameter) was cut into each half of the cell and masked with a sheet of 125 μm thick Kapton film applied to the interior of the shell using an epoxy (Hardman Part#4001) previously demonstrated to be compatible with lithium ion electrolytes. Cells of this construction were found to be stable for a minimum of 2 weeks after assembly. The negative electrode consisted of a 150 μm thick Li metal foil attached to 25 μm thick Cu foil. Two layers of glass microfiber separator (Whatman GF/A), infused with liquid electrolyte consisting of 1 M $LiPF_6$ in a 1:1 molar ratio of ethylene carbonate/dimethyl carbonate (EC/DMC), separated the negative and positive electrode. The total thickness of the stack from window to window is less than 1.2 mm. All cells were assembled under argon atmosphere.

***In Situ* Synchrotron X-ray Diffraction.** Data were collected at beamline X14A of the National Synchrotron Light Source (NSLS), Brookhaven National Laboratory, USA. The high photon flux (typically 9×10^{11} photon/s at ~17 keV focused beam, wavelength = 0.7293 Å) is beneficial for phase quantification. Full diffraction patterns were acquired in minutes with 0.005° angular resolution, using a 640 channel linear position-sensitive silicon detector with 3.2° full angular span. The detector was made by the NSLS detector group led by Peter Siddons. Raw data for each channel were recorded as I/I_0 x SF (scale factor), where I_0 is the beam intensity incident on the sample, I is the beam intensity reaching the Si strip detector after passing through the sample, and SF is a scale factor, defined as the maximum beam intensity of the I_0s. Normalization of diffraction patterns using the scale factor allows us to compare peak intensities between different scans regardless of the variation of beam intensity or data collection times. For galvanostatic tests, X-ray spectra were collected from 2θ = 7.4° to 18.6°; each scan took 6 min to acquire with good S/N ratio. For potentiostatic tests, a narrower 2θ range, 11.8°−15.0°, was collected to further improve the S/N ratio.

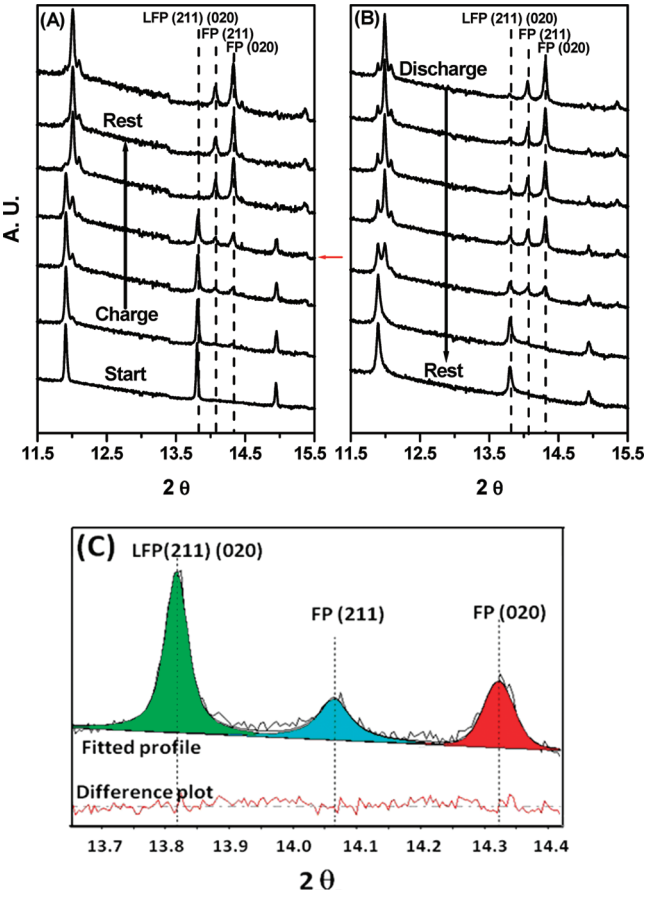

Figure 1. (A) *In situ* X-ray spectra for a cell of sample A galvanostatically charged at C/5 rate. The electrochemical state of each spectrum is labeled, and two spectra scanned before and after an open circuit rest are also shown for comparison. More than 120 scans were collected during one charge/discharge cycle; here every 10th scan is shown, and only a limited 2θ range of each scan is shown. (B) Similar spectra collected during galvanostatic discharge at C/5 rate. (C) Example of peak-fitting profiles and the corresponding difference plot, applied to the spectrum indicated by red arrow in (A).

Crystalline Phase Quantification. Figure 1 shows an example of sequential *in situ* spectra (every 10th spectrum is shown) collected during galvanostatic charging, rest, and discharge at C/5 rate, and the peak fitting and background-subtraction protocol. Typically, one spectrum was collected every 60 or 120 s during an experiment, resulting in dozens to hundreds of spectra

(8) Koyama, Y.; Chin, T. E.; Rhyner, U.; Holman, R. K.; Hall, S. R.; Chiang, Y.-M. *Adv. Funct. Mater.* **2006**, *16*, 492.
(9) Meethong, N.; Huang, H.-Y.; Carter, W. C.; Chiang, Y.-M. *Electrochem. Solid State Lett.* **2007**, *10*, A134.
(10) Meethong, N.; Huang, H.-Y.; Speakman, S. A.; Carter, W. C.; Chiang, Y.-M. *Adv. Funct. Mater.* **2007**, *17*, 1115.
(11) Meethong, N.; Kao, Y.-H.; Speakman, S. A.; Chiang, Y.-M. *Adv. Funct. Mater.* **2009**, *19*, 1060.
(12) Chung, S. Y.; Bloking, J. T.; Chiang, Y.-M. *Nat. Mater.* **2002**, *1*, 123.

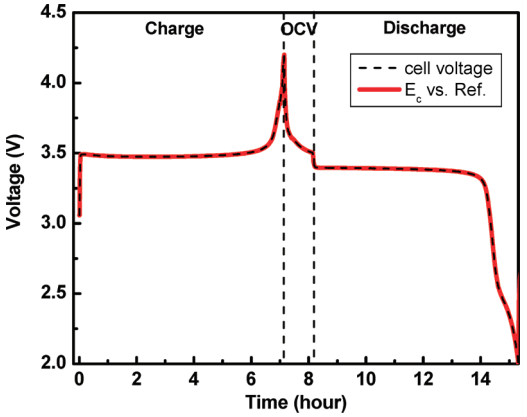

Figure 2. Results from a 3-electrode cell of the same construction as used in the in situ experiments, except for placement of a Li reference electrode between cathode and Li anode. Note that two curves are plotted. During charging and discharging at C/8 rate, it is seen that the cell voltage (dashed black line) and the voltage between the positive electrode and the lithium metal reference electrode (red line) differ negligibly. This shows that nearly all polarization occurs at the positive electrode and that the potential at the positive current collector can be represented by the cell voltage.

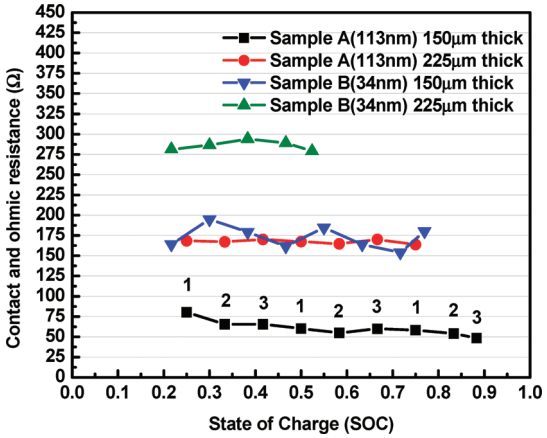

Figure 3. Sum of contact and ohmic resistance for the four electrode castings used in this study, measured from the voltage drop when cells undergoing 1C galvanostatic charging are periodically switched to different galvanostatic rates, C/5, C/10, or C/50, for 3 s. The resistance (R) is calculated as $R = (V_2-V_1)/(I_2-I_1)$. The test sequence is labeled for the sample of 113 nm particle size and 150 μm electrode thickness (black squares) as follows: Step 1 is when current is switched from 1C to C/5, step 2 is from 1C to C/10, and step 3 is 1C to C/20, respectively. The other curves shown followed the same sequence. The state of charge (SOC) shown here is based on the theoretical capacity of $LiFePO_4$ (170 mAh/g). It is seen that the sum of contact and ohmic resistances varies between the two powders and with electrode thickness but remains relatively constant with state-of-charge. The average resistance of each electrode over the tested range was used to calculate the voltage drop due to ohmic resistance during galvanostatic testing and subtracted from the total cell voltage to arrive at the overpotential.

depending on the C-rate. Peaks in the 2θ range 13.65°−14.425°, which includes the LFP(211)(020), FP(211), and FP(020) peaks, were used for phase quantification. An example of the linear background and Pseudo-Voigt function (PSF) peak shape fitting, along with the difference plot after fitting, is shown in Figure 1(C), accomplished with good residual value (<2%) using JADE 9.0 software. It is seen that the spectrum can be deconvoluted into three distinct peaks, the integrated intensities of which were used to compute phase fractions. (For sample A, the LFP(200) and FP(200) at 8.2°−8.4° and 8.63°−8.85°, respectively, are well-resolved and could also be used for quantification. Results using these peaks were in good agreement with those using the above peaks.)

The absolute amount of the LFP phase was normalized by using the LFP peak intensity in the initial scan for each cell as an internal standard. Quantification of the FP fraction is more problematic, as it may be miscalculated if amorphization occurs but is not taken into account. Here we galvanostatically charged cells at C/5 rate to 4.2 V and rested for several hours. The *in situ* measured FP peak intensities were assumed to represent 100% FP phase. If some amorphous phase remains after this procedure, a systematic overestimate of the amount of crystalline FP phase produced under other test conditions will result. In that instance, the amount of amorphous phase would be even greater than what is shown in the results.

Quantifying the Overpotential. In treating the experimental results, it is necessary to distinguish between the *overvoltage* and *overpotential*. The first is the amount by which the cell voltage exceeds the equilibrium or open-circuit voltage of the cell at any given state of charge. The overpotential, $\Delta\phi$, is the amount by which the potential experienced by the active material exceeds the equilibrium potential and can be quantified by subtracting the following potentials from the measured cell voltage: 1) the open-circuit (equilibrium) potentials for each sample relative to Li/Li^+ (previously determined to be about 8 mV higher for sample B than A[3]) and 2) potential drops due to resistive elements within the cell. In our cells the predominating potential drop occurs at the positive electrode. This was determined to be the case using a three-electrode configuration with a Li metal reference-electrode placed at the separator layer. Figure 2 shows two curves: the cell voltage, and the voltage between the reference and positive electrodes, during a full charge/discharge cycle. The fact that the two are indistinguishable from one another shows that the Li metal negative electrode has negligible polarization during these tests. Thus the cell voltage accurately gives the potential at the positive terminal.

The ohmic contributions originate from the porous matrix's inherent resistance and contact resistances such as between the current collector and electrode coating.[13] The matrix resistance depends on electrode composition and thickness and may vary with the SOC. For each sample, the sum of contact and ohmic resistances was determined during the initial charge cycle from changes in cell voltage upon stepwise changing the galvanostatic current. As shown in Figure 3, the ohmic resistance varies with electrode thickness and is two times higher for sample B at the same formulation and thickness but is constant with SOC in all electrodes. Subtraction of these ohmic-resistance voltage drops gives the instantaneous experimental overpotentials. Note that Ohm's law does not allow the entire electrode to be at the same potential as long as current is flowing. In these experiments we have attempted to minimize the potential drops across the electrode coatings by using thin coatings with low active materials loadings of 3.5 and 7 mg/cm^2, which are over a factor of 2 less than those used in even low impedance, high power, commercial Li-ion battery electrodes. These thin electrodes still contain enough active material to allow good signal-to-noise in the *in situ* X-ray measurements.

Diffuse-Interface (Phase-Field) Modeling. In order to interpret the overpotential- and size-dependent phase transition behavior, we have extended the diffuse-interface (phase-field) model of Tang et al.[4] In ref 4, *nucleation-limited* phase transition

(13) Srinivasan, V.; Newman, J. *J. Electrochem. Soc.* **2004**, *151*, A1517.

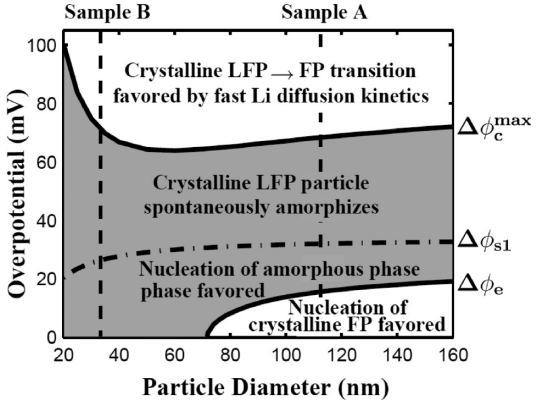

Figure 4. Phase transition map calculated from a phase-field model, showing the preferred phase transition pathways upon delithiation of a crystalline LFP particle as a function of the overpotential, $\Delta\phi$, and particle size. Results are calculated for 2% linear misfit strain, appropriate to crystalline $LiFePO_4$ (LFP) and $FePO_4$ (FP). The nucleation barrier for the crystalline-to-amorphous phase transition becomes smaller than that for the conventional crystalline phase transformation at $\Delta\phi > \Delta\phi_e$ and vanishes at $\Delta\phi_{s1}$, permitting spontaneous amorphization. Growth of the crystalline FP phase becomes preferred at $\Delta\phi > \Delta\phi_c^{max}$ due to Li diffusion-limited crystallization that is faster than the rate of structural disordering. (Note that the horizontal axis here differs from a previous result, Figure 10 in ref 4, by a factor of 2, this being the particle diameter as opposed to particle radius.)

pathways were modeled as a function of particle size, overpotential, and misfit strain (between the pre-existing and nucleated crystalline phases). Here, we extend the model to also consider *growth-limited* transitions, which are expected to become more significant at large overpotentials where nucleation is expected to become very facile and growth kinetics may determine which phase transition becomes dominant. The model applies to instances where the metastable amorphous phase has lower surface energy than its crystalline alternative, and we have specifically modeled the delithiation (charging) transition.

The chemical free energy of a homogeneous Li_cFePO_4 as a function of c and temperature was given in ref 4. If the nucleation barriers for the crystalline FP phase and the metastable amorphous phase are both sufficiently large, it is always possible for the solid solution to form metastably instead - the free energy of the solid solution increases following the free energy curve, and at the spinodal point, which the function in ref 4 indicates occurs at ~45 mV overpotential and c~0.12, phase separation by spinodal decomposition occurs. This possibility was also recently discussed by Ceder.[14] The likelihood of a metastable solid solution increases as the lithium miscibility gap shrinks with crystallite size reduction[9] or doping and atomic disorder.[11,15,16] However, in the present undoped materials, we have not seen evidence for extended solid solutions forming during *in situ* charging experiments at rates up to 5C (e.g., Figure 7 shows results for 34 and 220 nm at 1C charge rate). Thus, here we focus on the competing pathways of crystalline FP nucleation and amorphization.

The results of the phase field model, calculated using materials parameters appropriate to $Li_{1-x}FePO_4$,[4] can be displayed as a map of the preferred phase transformation pathway in a $\Delta\phi$ - particle size coordinate system, Figure 4, for comparison with experimental data. The activation energy for nucleating the amorphous phase decreases with decreasing particle size and increasing overpotential, $\Delta\phi$, and the crystalline-to-amorphous phase transition becomes preferred above a critical value of overpotential, $\Delta\phi_e$, which at large particle sizes is calculated to be ~20 mV (equivalent to an undercooling of ~230 K for a thermal phase transition). The model also predicts that $\Delta\phi_e$ decreases with particle size and vanishes below a critical size of 70 nm (Figure 4). These results were previously described (see Figure 10 in ref 4). However, by including growth kinetics in the model, Figure 4 illustrates a new prediction wherein above another critical overpotential, $\Delta\phi_c^{max}$, the crystalline-to-crystalline phase transition pathway is again preferred. As we show, this result is supported by experiment. (Note also that Figure 4 is plotted against particle diameter, whereas Figure 10 in ref 4 is plotted against particle radius.) A basic description of the phase-field model follows; additional details may be found in refs 4 and 14.

I. Field Variables and Free Energy Formulation. The physical state of a $LiFePO_4$ particle is characterized by three field variables:

1) Local lithium concentration $c(\vec{r})$ $(0 < c < 1)$;
2) Local crystallinity $\eta(\vec{r})$ that represents the local structural order of the $FePO_4$ framework. $\eta = 1$ − perfectly crystalline phase; $\eta = 0$ − disordered structure.
3) Local displacement field $\vec{u}(\vec{r})$ that characterizes the elastic strain field in the particle.

We assumed a core−shell phase transition geometry,[13] and isotropic approximations are applied to the thermodynamic, elastic, and kinetic properties of $LiFePO_4$ olivines. This assumption is in part for mathematical convenience, but we note that the core−shell configuration is more likely to occur for the amorphization transition due to the isotropic surface energy of the amorphous phase, especially if its surface energy is less than that of all crystalline orientations. As pointed out in ref 10 and observed in ref 17, a core−shell geometry is not expected for the crystalline transformation. The total free energy of a spherical $LiFePO_4$ particle is postulated to be a functional of the field variables

$$F_{tot}[c(r),\eta(r),u(r)] = \int\int\int dV\left[f_{chem}(c,\eta) + f_{el}(u,du/dr,c,\eta) + \frac{\kappa^2}{2}\left(\frac{\partial c}{\partial r}\right)^2 + \frac{\nu^2}{2}\left(\frac{\partial \eta}{\partial r}\right)^2\right] + 4\pi R^2\gamma(\eta_s) \quad (1)$$

where R is particle radius, and $u(r)$ is the radial component of the displacement vector field. F_{tot} consists of energy contributions from the following:

1) The homogeneous chemical free energy, $f_{chem}(c,\eta)$, represents the free energy density of Li_cFePO_4 with a uniform Li concentration c and structural order η in the absence of elastic strains. It is modeled by a regular solution formulation[4]

$$f_{chem}(c,\eta) = \{f^{FP}(\eta)(1-c) + f^{LFP}(\eta)c + RT[c\ln c + (1-c)\ln(1-c)] + [W_s p(1-\eta) + W_a p(\eta)]c(1-c)\}/V_m \quad (2)$$

where V_m is the molar volume of $LiFePO_4$, and W_s and W_a are the regular solution coefficients for

(14) Ceder, G.; Mailk, R. The 15th International Meeting on Lithium Ion Batteries, IMLB2010, Abstract #327.
(15) Meethong, N.; Kao, Y.-H.; Carter, W. C.; Chiang, Y.-M. *Chem. Mater.* **2010**, *22*, 1088.
(16) Gibot, P.; Casas-Cabanas, M.; Laffont, L.; Levasseur, S.; Carlach, P.; Hamelet, P.; Tarascon, J.-M.; Masquelier, C. *Nat. Mater.* **2008**, *7*, 741.
(17) Tang, M.; Carter, W. C.; Chiang, Y.-M. *Annu. Rev. Mater. Res.* **2010**, *40*, 501.

crystalline and amorphous Li_cFePO_4, respectively. $p(\eta) = (1-\eta)^3(1+3\eta+6\eta^2)$ is a smooth interpolation function between $p(\eta = 0) = 1$ and $p(\eta = 1) = 0$. $f^{FP}(\eta)$ and $f^{LFP}(\eta)$ are the chemical free energy density of stoichiometric $FePO_4$ and $LiFePO_4$ and are given the following expressions

$$f^{FP}(\eta) = f^{FP}(\eta = 1) + \Delta f^{FP,c\rightarrow a} p(\eta) + \frac{a_{FP}^2}{2}\eta^2(1-\eta)^2$$

$$f^{LFP}(\eta) = f^{LFP}(\eta = 1) + \Delta f^{LFP,c\rightarrow a} p(\eta) + \frac{a_{LFP}^2}{2}\eta^2(1-\eta)^2 \quad (3)$$

where $\Delta f^{FP,c\rightarrow a}$ ($\Delta f^{LFP,c\rightarrow a}$) is the vitrification free energy change of $FePO_4$ ($LiFePO_4$), and a_{FP}^2 (a_{LFP}^2) is the free energy barrier between amorphous and crystalline $FePO_4$ ($LiFePO_4$).

2) Elastic strain energy, f_{el}, arises from the coherency stress field across the $LiFePO_4/FePO_4$ interface during a crystalline-to-crystalline phase transition

$$f_{el} = (K/2 - G/3)\left(\frac{du}{dr} + 2\frac{u}{r} - 3e^0(c,\eta)\right)^2 + G\left(\frac{du}{dr} - e^0(c,\eta)\right)^2 + 2G\left(\frac{u}{r} - e^0(c,\eta)\right)^2 \quad (4)$$

where K and G are the orientation-averaged bulk and shear moduli of $LiFePO_4$, and $e^0(c,\eta) = \Delta e^0\,(1-c)\,p(1-\eta)$ is the stress-free strain with $\Delta e^0 \equiv e^0(c = 1,\eta = 1) - e^0(c = 0,\eta = 1)$ being the linear misfit strain between crystalline $FePO_4$ and $LiFePO_4$. We assume, however, that the elastic energy upon a crystalline-to-amorphous phase transition is negligible.

3) Gradient energies, $\kappa^2/2(\partial c/\partial r)^2$ and $\nu^2/2(\partial\eta/\partial r)^2$, contribute to the interface energy of crystalline $FePO_4/LiFePO_4$ and crystalline/amorphous phase boundaries.

4) Particle surface energy, $\gamma(\eta_s)$, is postulated to be a simple function of surface crystallinity η_s: $\gamma(\eta_s) = \Delta\gamma\eta_s^2$. $\Delta\gamma \equiv \gamma(\eta_s = 1) - \gamma(\eta_s = 0)$ is the surface energy difference between crystalline and amorphous $LiFePO_4$.

The parameters appearing in the free energy expression eq 1 have been qualitatively assessed for $LiFePO_4$. A table of parameter values used in the calculations can be found in ref 4.

II. Nucleation Energy Barrier Calculations. Upon delithiation, three (meta)stable bulk phases exist in the phase-field model, which are crystalline $LiFePO_4$ (cLFP) and $FePO_4$ (cFP) as well as a delithiated amorphous phase (aFP). The Li concentration $c(r)$, crystallinity $\eta(r)$, and displacement $u(r)$ fields of each bulk phase locally minimizes a particle's excess free energy with respect to the surrounding Li reservoir at a fixed Li chemical potential μ_{Li}^e

$$\Delta F_{tot} = F_{tot}[c(r),\eta(r),u(r)] - \int\int\int \mu_{Li}^e c(r)dV \quad (5)$$

The magnitude of μ_{Li}^e is directly specified by the applied overpotential $\Delta\phi$: $\mu_{Li}^e = -F(\phi_{coex} + \Delta\phi)$, where F is the Faraday constant, and $\phi_{coex} = 3.45$ V is the electrical potential at which cLFP and cFP coexist in equilibrium.

In addition to the locally stable mathematical solutions for $c(r)$, $\eta(r)$, and $u(r)$ that represent the bulk phases, two overpotential-dependent saddle-point solutions that are stationary to ΔF_{tot} can also be obtained from the model -- they correspond to the critical nucleus states for the crystalline-to-crystalline (cLFP→cFP) and crystalline-to-amorphous (cLFP→aFP) phase transitions, respectively.[4] The nucleation energy barriers associated with the two competing phase transformations are given by the free energy difference between these critical nucleus states and the cLFP phase

$$\Delta F_{c\rightarrow c} = \Delta F_{tot}(\text{cLFP} \rightarrow \text{cFP}) - \Delta F_{tot}(\text{cLFP})$$

$$\Delta F_{c\rightarrow a} = \Delta F_{tot}(\text{cLFP} \rightarrow \text{aFP}) - \Delta F_{tot}(\text{cLFP}) \quad (6)$$

Additionally, our model predicts under certain conditions the formation of (meta)stable surface phases known as "surficial amorphous films" (SAFs), known to form in numerous other crystalline systems.[18] SAFs with a nanoscale equilibrium thickness have recently been observed on olivine particles.[19] Our calculations show that the presence of SAFs on particle surface promotes the crystalline-to-amorphous bulk phase transition. The details are present elsewhere.[4,17]

III. Delithiation Kinetic Simulations. Delithiation of a cLFP particle involves Li diffusion as well as structural disordering within the particle if the amorphous phase transition occurs. In the phase-field model, the Li diffusion process is modeled by the Cahn−Hilliard equation[20]

$$\frac{\partial c}{\partial t} = \nabla\cdot(M_{Li}c(1-c)\nabla\mu_{Li}) \quad (7)$$

where M_{Li} is the Li mobility, and $\mu_{Li} = \delta F_{tot}/\delta c$ is the local Li chemical potential. The structural disordering process is modeled by the Allen-Cahn equation[21]

$$\frac{\partial\eta}{\partial t} = -M_{am}\frac{\delta F_{tot}}{\delta\eta} \quad (8)$$

where M_{am} is the mobility of the crystalline/amorphous interface. As the relaxation of the elastic field usually occurs at a much smaller time scale than diffusion and structural evolution processes, mechanical equilibrium is assumed to be maintained throughout delithiation, i.e.

$$\frac{\delta F_{tot}}{\delta u} = 0 \quad (9)$$

To simulate the delithiation process under a constant overpotential, i.e., corresponding to a PITT test, we apply the following boundary condition at the particle surface, $r = R$

$$J_{Li}|_{r=R} = \beta(\mu_{Li}(r = R) - \mu_{Li}^e) \quad (10)$$

where the Li surface flux $J_{Li}|_{r=R}$ is proportional to the difference between the Li local chemical potentials at particle surface, $\mu_{Li}(r = R)$, and in the surrounding electrolyte, $\mu_{Li}^e = -F(\phi_{coex} + \Delta\phi)$. A sufficiently large value is chosen for the Li surface exchange rate coefficient β to ensure that Li surface insertion/deinsertion imposes no kinetic limitation on the delithiation process. In addition to eq 10, natural boundary conditions for c, η, and u derived from calculus of variation are applied at particle surface and center to close

(18) Luo, J.; Chiang, Y.-M. *Annu. Rev. Mater. Res.* **2008**, *38*, 227.
(19) Kayyar, A.; Qian, H.; Luo, J. *Appl. Phys. Lett.* **2009**, *95*, 221905.
(20) Cahn, J. W.; Hilliard, J. E. *J. Chem. Phys.* **1958**, *28*, 258.
(21) Allen, S. M.; Cahn, J. W. *Acta Metall.* **1979**, *27*, 1085.

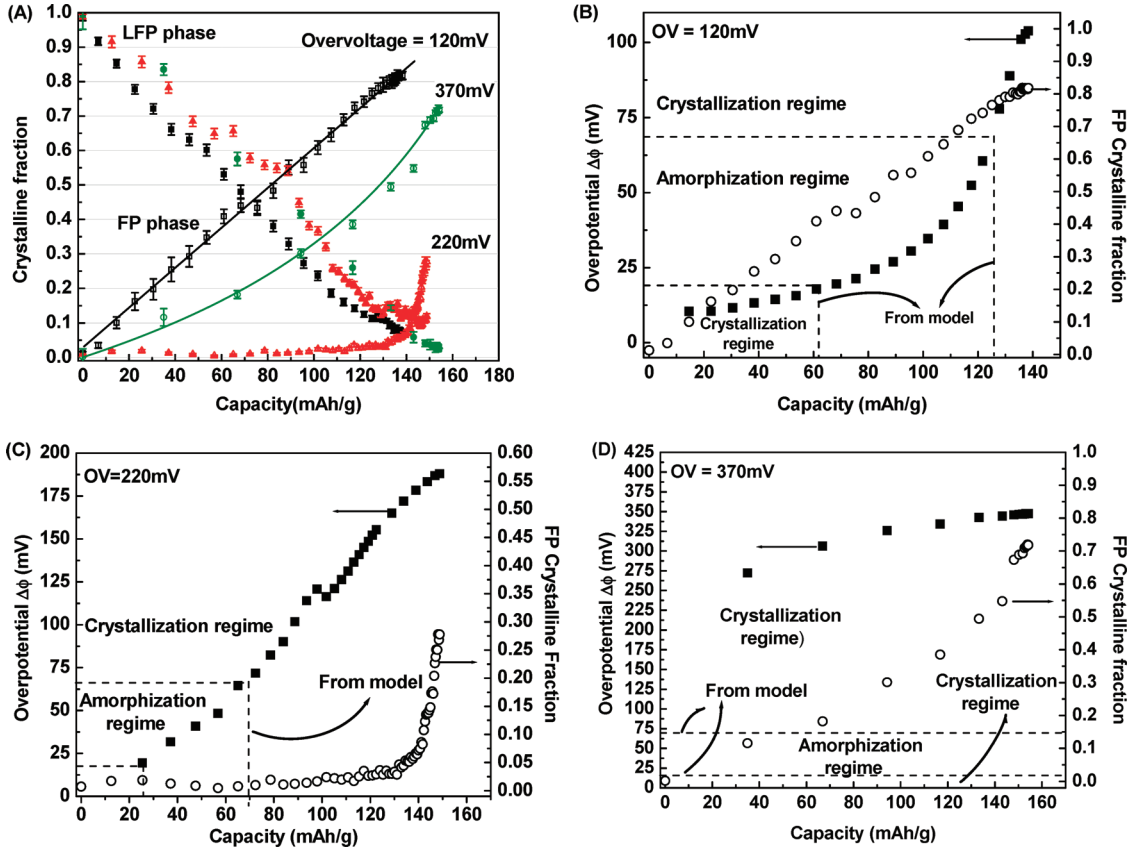

Figure 5. *In situ* synchrotron XRD measurement of phase fractions for sample A, of 113 nm mean particle size, during the first cycle of potentiostatic charging. (A) Overvoltage dependence of LFP (solid symbol) and FP (open symbol) crystalline fractions, in electrodes of 225 μm thickness. The overvoltage is calculated by subtracting the LFP/FP equilibrium potential vs Li/Li^+, measured in ref 3, from the cell voltage. While all three cells show a linear decrease in LFP fraction with charge capacity, the increase in FP fraction is strongly dependent on potentiostatic voltage. Parts (B-D) plot the ohmic-resistance-corrected overpotentials, $\Delta\phi$, vs SOC for overvoltages 120, 220, and 370 mV. The filled squares show variation in $\Delta\phi$ with specific charge capacity, while the open circles show the corresponding fraction of crystalline $FePO_4$ (FP). The dashed lines refer to results from the phase-field model, see Figure 4 and text.

the system of equations eqs 7-9

$$\left.\frac{\partial c}{\partial r}\right|_{r=R} = 0,\ \left.\frac{\partial \eta}{\partial r}\right|_{r=R} + \gamma'(\eta_s)/\nu^2 = 0,\ \left.\frac{\partial c}{\partial r}\right|_{r=0} = \left.\frac{\partial^3 c}{\partial r^3}\right|_{r=0} = \left.\frac{\partial \eta}{\partial r}\right|_{r=0} = 0 \quad (11)$$

The delithiation simulations reveal that a shift in the phase transition pathway from cLFP→aFP to cLFP→cFP occurs when $\Delta\phi$ is raised above a characteristic overpotential $\Delta\phi_c$ (Figure 4). The magnitude of $\Delta\phi_c$ increases with the mobility ratio M_{am}/M_{Li}. While the Li mobility M_{Li} can be evaluated from the Li diffusion coefficient, the magnitude of M_{am} for $LiFePO_4$ is less certain. Nevertheless, an upper bound estimate, $\Delta\phi_c^{max}$ which is the limiting $\Delta\phi_c$ value as $M_{am}/M_{Li} \to \infty$, can be obtained for $\Delta\phi_c$ from the simulations.[17] The $\Delta\phi_c$ curve in Figure 4 corresponds to these conditions.

Experimental Results and Discussion

Potentiostatic Tests. We first discuss results from potentiostatic measurements, in which a fairly wide range of overpotential, $\Delta\phi$, was accessible by varying the cell voltage. Note that $\Delta\phi$ is not constant during a potentiostatic hold, since the current and related ohmic drops vary with time. Meethong et al.[9] previously measured the multiphase-equilibrium potential of the present sample materials using galvanostatic titration and found that it differs slightly between samples A and B (being 3.430 V and 3.438 V, respectively[3]). The compositional width of the lithium miscibility gap decreases with particle size,[9] thus increasing the SOC range where a continuously varying single-phase/solid-solution equilibrium potential exists. To study the onset of phase transformations, we first charged the test cells to the limiting solid-solution concentration. A galvanostatic intermittent titration (GITT) protocol with C/10 current pulses producing 2 to 3.4 mAh/g capacity steps was applied, after each of which cell voltages were relaxed under open-circuit conditions. The single phase $Li_{1-x}FePO_4$ composition limit is reached when the open-circuit voltage (OCV) reaches the "plateau" voltage. The cell voltage was then stepped to a new potentiostatic value at which time-dependent current was measured. These and the ohmic resistance (Figure 3) determine $\Delta\phi$ versus SOC. Simultaneously, X-ray spectra were collected until the potentiostatic current had decayed to C/50.

The *in situ* potentiostatic measurements resulted in results such as those in Figures 5 and 6 showing evolution of the LFP/FP phase fractions upon the first charge (delithiation). For each material, the three cells were made from electrodes punched from a single coating. Figure 5A plots results for sample A at overvoltages (OV) of 120 mV, 220 mV, and 370 mV. The LFP fraction, f_{LFP}, decreases approximately

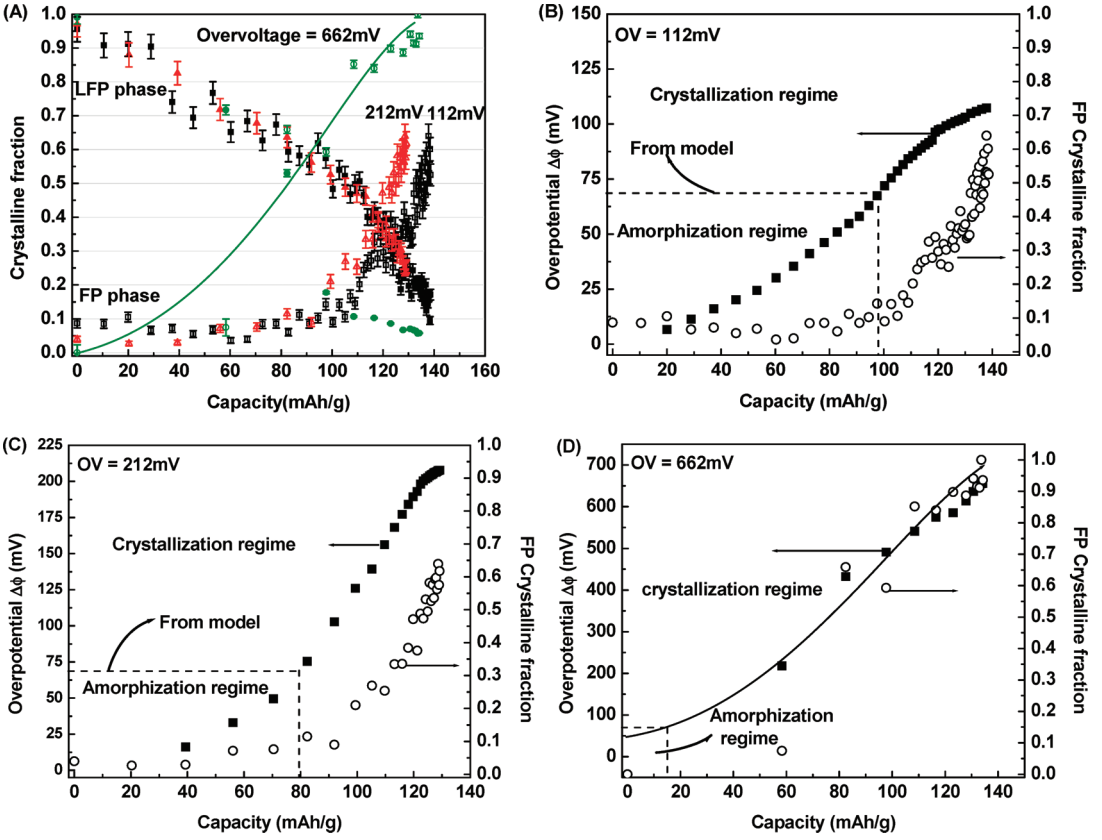

Figure 6. *In situ* synchrotron XRD measurement of phase fractions for sample B, of 34 nm mean particle size, during the first cycle of potentiostatic charging. (A) Overvoltage dependence of LFP (solid symbol) and FP (open symbol) crystalline fractions, in electrodes of 225 μm thickness. Delayed crystallization of FP with respect to charge capacity indicates that amorphization is the predominant transition for this particle size at low overpotentials. (B) Overpotential ($\Delta\phi$) dependence of the FP crystalline fraction, at overvoltage = 112 mV. The overpotential is calculated by subtracting the LFP/FP equilibrium potential and the potential drop due to ohmic and contact resistance from the cell voltage. (C) Overpotential dependence of the FP crystalline fraction, at overvoltage = 212 mV. (D) Overpotential dependence of the FP crystalline fraction, at overvoltage = 662 mV. Dashed lines refer to results from the phase-field model, see Figure 4 and text.

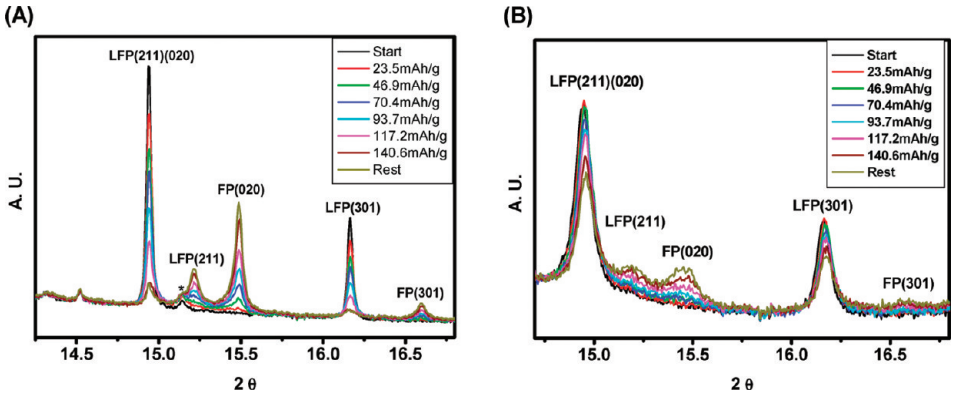

Figure 7. In situ X-ray diffraction patterns collected during 1C rate charge with scans taken at 2 min intervals over the 2θ range shown; at 16 keV (0.7738A). (A) 220 nm particle size and (B) 34 nm particle size sample, denoted sample B in text. The coarsened sample in (A) was obtained by heat treating sample B at 800 °C for 5 h in Ar atmosphere. Note that (B) exhibits broader peaks and a systematic shift of both the LFP and FP peaks during charging as well as an increase in the background intensity in the 2θ range 15−16°. In contrast, there is no significant peak shift in (A) during charging. "*" in (A) indicates a peak from an electrochemically inactive impurity phase, the intensity and position of which does not change during charging.

linearly with increasing charge capacity at each voltage. The corresponding FP fraction, however, shows different evolution behavior at each potentiostatic voltage.

- At OV = 120 mV, the FP-fraction, f_{FP}, has a corresponding linear increase—consistent with $f_{LFP} + f_{FP} = 1$. This is "conventional" behavior in which only the two crystalline phases are present, and their respective fractions obey the binary lever rule.
- At OV = 220 mV, a markedly different behavior is observed: no FP phase is detected until a ~67% state of charge occurs (100% SOC corresponds to the complete removal of lithium, $x = 1$, equivalent to 170 mAh/g of specific capacity). When the potentiostatic charge was terminated, the SOC was ~82%—*however*, f_{FP} corresponded to only 30% and $f_{LFP} + f_{FP} = 0.4$. We conclude that the

remaining 60% of the $Li_{1-x}FePO_4$ *must be noncrystalline*. (Note that particle size broadening was taken into account in quantifying the phase fractions).

- At the largest overvoltage, 370 mV, the phase-fraction vs SOC behavior is *intermediate* between that at 120 and 220 mV. At all SOC, the sum $f_{LFP} + f_{FP} < 1$, indicating presence of amorphous phase, and when potentiostatic charging is complete $f_{LFP} + f_{FP} \approx 0.7$, indicating ~30% residual amorphous phase.

The striking conclusion is that the crystalline-to-crystalline phase transition appears to be preferred at both low (120 mV) and high (370 mV) overvoltage, while amorphization dominates at the intermediate overvoltage (220 mV). We know of no previous experimental or theoretical results suggesting such an effect.

Upon subtracting ohmic resistance from the overvoltages (OV) to obtain the overpotential, $\Delta\phi$, a more detailed correlation between $\Delta\phi$ and the preferred phase transition pathway emerges. The data from OV = 120, 240, and 370 mV have been replotted in Figure 5 (113 nm particles) against $\Delta\phi$. In each case, the first 10 s of data have been removed to exclude possible spurious results due to high initial capacitive currents. We emphasize the correlation between the value of the overpotential at the beginning of charge (i.e., at low capacity) and the phase transition pathway. For the lowest overvoltage (OV = 120 mV), Figure 5B plots the crystalline FP fraction (open symbols) and $\Delta\phi$ (closed symbols) against charge capacity (mAh/g). Note that FP crystallizes immediately upon charging and increases linearly with SOC. Simultaneously, $\Delta\phi$ remains below 20 mV until the electrode is about half-charged and then rises sharply until it ultimately approaches the limiting value of 120 mV. Plotted as dashed lines in Figure 5B are the critical overpotentials below and above which the crystalline-to-crystalline transition is preferred, based on the model (Figure 4). We see that the overpotential starts in and remains in the crystallization region until 60 mAh/g of charge capacity has accrued (35% SOC). Correspondingly, the preferred phase transition is to the crystalline FP phase, even as the overpotential traverses the regime where amorphization is preferred. One expects that once crystallization of FP has initiated, it is able to continue due to the presence of many crystalline nuclei.

In contrast, at OV = 220 mV, Figure 5C, the overpotential (closed symbols) is almost immediately in the amorphization regime. Correspondingly, the crystalline FP fraction (open symbols) remains near zero until more than 100 mAh/g of charge capacity has accrued (~60% SOC). Figure 5A shows that the LFP fraction (closed triangles) is decreasing linearly during this process. Clearly, mass balance requires the presence of another phase that is not detectable by X-ray diffraction (e.g., Figure 1) − an amorphous phase.

At the highest overvoltage, OV = 370 mV, the overpotential rises immediately to the second crystallization regime at high overpotentials (see also Figure 4). Correspondingly, the FP fraction increases immediately upon charge, while the LFP fraction again decreases linearly with SOC (Figure 5A). The increase in FP with SOC is less steep than is expected from the binary lever rule, suggesting that some amorphous phase is present even though crystallization of FP dominates. Thus we conclude that the preferred phase transformation sequence depends on $\Delta\phi$ and favors the amorphous phase at intermediate values of $\Delta\phi$.

Results from a single sample may not be considered fully convincing, and therefore we now refer to Figure 6, which shows results for Sample B (34 nm) at OV = 112, 212, and 662 mV. At this particle size of 34 nm, Figure 4 predicts that amorphization is the preferred transition pathway from zero overpotential until the upper critical overpotential is reached at about $\Delta\phi$~70 mV. Figure 6A shows that upon charge, the LFP fraction at all three overvoltages decreases with SOC but not linearly as would be the case if all extant phases are crystalline. The greater-than-expected LFP fraction could be explained by a metastable delithiated solid solution of LFP; this possibility is discussed below with respect to Figure 7. For sample B, at all three overvoltages, the FP fraction is negligible for charge capacity up to about 60 mAh/g (~35% SOC). Thereafter, the crystallization of FP, or lack thereof, depends on the value of the overpotential. In Figure 6B-D, the results are again plotted vs ohmic-resistance-corrected overpotential, $\Delta\phi$. In Figure 6B (OV = 112 mV), the overpotential remains in the amorphization regime until 100 mAh/g of charge capacity has accrued. Correspondingly, the FP fraction remains low at ~0.1 within this regime. However, once $\Delta\phi$ exceeds 70 mV, entering the crystallization regime, a sharp increase in the crystalline FP fraction is observed. In Figure 6C (OV = 212 mV), the result is similar. The crystalline FP fraction remains low while $\Delta\phi$ remains within the amorphization regime and then rises sharply once $\Delta\phi$ enters the crystallization regime. In Figure 6D (OV = 662 mV), the initial overpotential cannot be determined accurately due to capacitive current transients. However, it is clear when the FP fraction begins to rise sharply at ~40% SOC, $\Delta\phi$ is well above 200 mV and remains in the crystallization regime thereafter. Note that only for the OV = 662 mV experiment does the final FP fraction approach unity, despite the charge capacities being similar in all three cases. Thus, a large overpotential produces a more complete transformation to crystalline FP in these nanoscale particles.

We explored the question of metastable solid solution formation by monitoring peak shifts during the *in situ* experiments, since these reflect changes in unit cell parameters that are in turn correlated with composition via the Vegard's law relationship for this material. Figure 7 compares *in situ* diffraction spectra collected during 1C rate charging of Sample B at its initial 34 nm particle size (Figure 7(B)) and after coarsening to 220 nm (Figure 7(A)). For the 220 nm particle size sample, neither the LFP nor FP peaks shift noticeably as a function of state of charge. This was also the case for Sample A (113 nm) and indicates minimal solid solution formation, consistent with the equilibrium phase diagram for coarse samples. However, for the 34 nm particle size sample, both the LFP and FP peaks shift systematically to higher 2θ with increasing SOC. For the LFP, this is

consistent with delithiation (shrinking unit cell volume). For the FP, this suggests that the initially formed phase is supersaturated with Li and then evolves toward a more delithiated composition. At the same time, the background intensity in Figure 7(B) can be seen to increase, consistent with the formation of amorphous phase. For both crystalline phases, the magnitude of the peak shift translates to a variation in Li content of ~5%. The positive deviation from linearity of the LFP fraction vs SOC in Figure 6(A) could be explained by nonstoichiometry of this order in the LFP. The continuous peak shift with SOC in Figure 7(B) indicates that the compositions are not "pinned" while in coexistence with each other and the amorphous phase, however. We conclude that while charging does produce detectable variations in solid solution in the 34 nm particle size sample, these are not so extensive as to suggest that metastable crystalline solid solutions are a primary phase transition pathway. This was true in the present study for charge rates up to 3C; still higher charge rates could produce different results under higher overpotentials. Regarding the effect of particle size, here we are able to compare sizes of 34 nm, 113 nm, and 220 nm and find that the results fall remarkably close to what is predicted in Figure 4.

The experiment and the model are consistent with each other, despite simplifying assumptions in the model such as 1) the particle shapes are spherical (this is nearly the case for sample B, A is more anisometric[3,9]); 2) interfacial energies are isotropic (valid for the amorphous phase only [22]); 3) the amorphous phase uniformly coats the particle; and 4) lithium diffusion in the crystalline phase is isotropic. Note that no adjustments of the materials parameters were carried out to improve fit to the experiments; the exact same values are used to produce the results in Figure 4 as were previously used in ref 4. The prediction that the crystalline-to-crystalline phase transition is preferred (i.e., has a smaller activation energy) below a critical value of overpotential, $\Delta\phi_{crit}$ (~20 mV for large particles) is consistent with the experimental results for sample A (113 nm, Figure 5B). The prediction that $\Delta\phi_e$ decreases with particle size and vanishes below a critical size of 70 nm (Figure 4) is consistent with the results for sample B (34 nm, Figure 6).

The new prediction of a secondary crystalline-to-crystalline phase transition pathway above a critical overpotential, $\Delta\phi_c^{max}$, is also supported by the experimental data (Figure 5D and Figure 6). This behavior originates in part from an interesting feature of electrochemically driven phase transitions that differs from thermal phase transitions. In most thermal phase transitions, the driving force increases with undercooling, but simultaneously the transformation kinetics become more sluggish as temperature decreases. In electrochemically driven phase transitions, which may take place under isothermal conditions or even produce a temperature rise (e.g., self-heating) the kinetics need not decrease as the driving force increases (larger overpotential). Comparing the two competing transformation pathways, at larger overpotentials ($> \Delta\phi_{s1}$), nucleation of the amorphous phase is expected to become very facile, hence its growth may become rate-limiting. In addition, a higher overpotential should generate a larger Li^+ out-flux from the particles while having no direct effect on the structural disordering kinetics. In contrast, in the crystalline−crystalline transformation where the relative atomic positions are fixed, the crystalline LFP to delithiated amorphous transition requires coupled lithium diffusion and structural disordering at the growth front. At sufficiently large overpotentials, the structural disordering process becomes slow compared to lithium diffusion. As a result, the direct crystalline phase transformation, which can be accommodated by lithium diffusion alone, reemerges as the preferred transition.

The results in Figure 4 contain one additional critical overpotential, $\Delta\phi_{s1}$, above which it is predicted that the amorphization reaction is not only favored but is spontaneous (i.e., the nucleation barrier vanishes). The current experiments do not test this transition; it cannot be resolved whether the amorphization transition is spontaneous or thermally activated.

Galvanostatic Tests. Practical use of rechargeable batteries is of course not limited to potentiostatic operation. We also conducted *in situ* galvanostatic tests of both samples, during which the overpotential and phase fractions were simultaneously measured. One series of results, in which sample A tested at C/5, 1C, and 2.6C rates, is shown in Figure 8. Consistent with the potentiostatic experiments, these show that f_{FP} is lowest at intermediate (1C) charge rate corresponding to an intermediate $\Delta\phi$. At both lower and higher C-rates (and $\Delta\phi$), crystallization of FP is enhanced. Moreover, at all C-rates, a sharp increase in crystallization is observed at large SOCs when $\Delta\phi$ is the highest.

These results imply the possibility of complete amorphization when cycling over selected ranges of overpotential or state-of-charge or at selected galvanostatic rates. Figure 9 shows the outcome of two such experiments. In Figure 9A, sample A was first cycled for 4 cycles at a 1C rate and then at 5C rate for an additional 4 cycles. At the 1C rate, f_{LFP} oscillates within each cycle but diminishes with sequential cycles. The detected f_{LFP} in the first cycle was negligible because the sample was only charged to 50% SOC before discharging. Thereafter, the f_{FP} increases during charge but never exceeds 40%. At a 5C rate, however, both crystalline phase fractions diminish sharply and remain below 20% throughout cycling. The capacity obtained during each cycle is also shown in the figure; the Coulombic efficiency was >98% for all cycles. Results for sample B (Figure 9B) show similar oscillations in f_{LFP} and f_{FP} during 1C cycling, but upon 5C cycling, virtually no FP phase is detectable, and the LFP fraction is only a few percent. The transmission synchrotron diffraction experiments average over the electrode thickness—this includes at least some potentially active material that is not cycled at the higher rates. We conclude that some active material is not contributing to measured capacity, based on the following observations. The 5C rate capacity is reduced to 90−100 mAh/g in both samples (Figure 9); thus about one-third of the

(22) Wang, L.; Zhou, F.; Meng, Y. S.; Ceder, G. *Phys. Rev. B* **2007**, *76*, 165435.

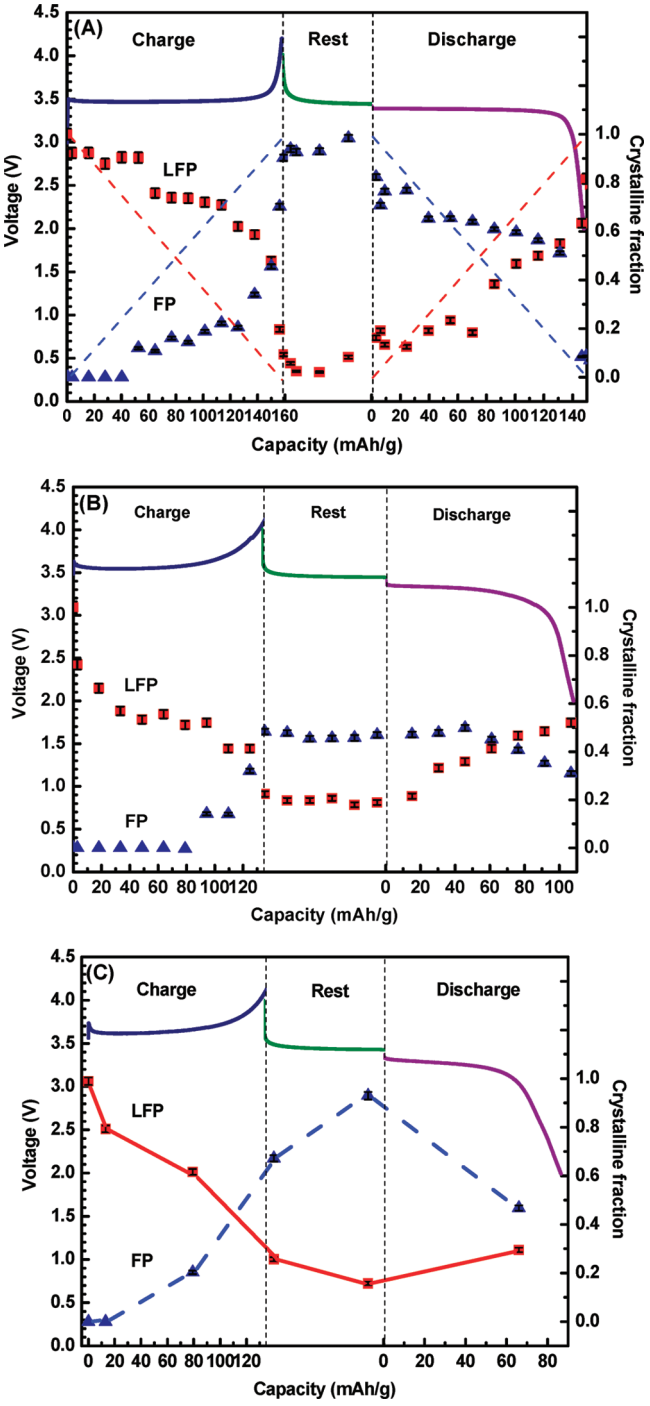

Figure 8. *In situ* synchrotron XRD of sample A during the first galvanostatic charge, rest [30 min], and discharge cycles. (A) At C/5 rate, the phase fractions do not evolve linearly with capacity as expected from simple two-phase immiscibility (straight dashed lines). Crystallization of FP accelerates toward the end of charge (discharge) where the overpotential is highest (lowest). (B) Similar behavior is seen at 1C rate, except that greater amorphization is indicated by the fact that the FP fraction reaches only ~0.5 at ~80% SOC (135 mAh/g charge capacity). After charging, the sum of LFP and FP fractions is only ~70%, and at the end of discharge, it is ~80%. (C) At 2.6C rate, data points are sparse due to the short time interval between spectra but show higher FP crystallization rate at the correspondingly higher overpotential. Note also that during the rest, FP crystallization appears to continue when the overpotential is removed.

electrode is not active. The size distribution for sample A (113 nm)[9] includes coarser particles that may not be electrochemically active at this cycling rate. This explains

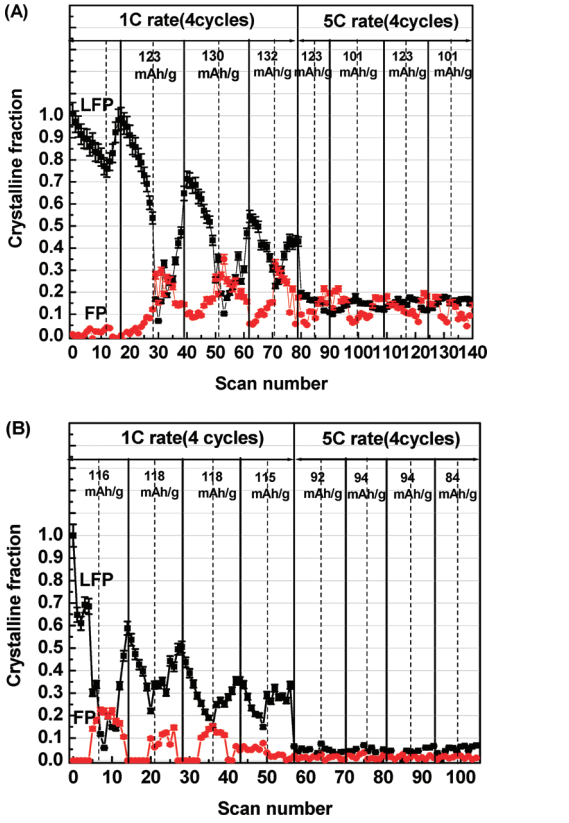

Figure 9. *In situ* synchrotron XRD measurement of phase fractions during galvanostatic cycling at 1C rate for four cycles followed by 5C rate for four cycles. The reversible capacity is labeled for each cycle. (A) Sample A of 113 nm mean particle size and (B) Sample B of 34 nm mean particle size. Both show oscillating but decreasing LFP and FP crystalline fractions during 1C cycling, which however diminish sharply upon 5C cycling, showing that it is primarily the transformed amorphous phase that is being cycled.

why the residual crystalline LFP fraction remains essentially unchanged during 5C cycling (Figure 9A). The FP fraction in sample A does oscillate slightly during these cycles, indicating that some of the crystalline phase is active. Note that in both samples, the measured capacity at 5C rate cannot be explained by the amount of crystalline phase present. This shows unequivocally that the amorphous phase is electrochemically active; in fact it contributes most of the observed reversible capacity.

We have focused on the phase transition during charging, corresponding to the delithiation of $LiFePO_4$ toward $FePO_4$ olivine. Amorphization of this product phase is not surprising given its structural similarities to good glassformers such as SiO_2. Although here we observe only the olivine polymorph, $FePO_4$ does have a stable quartz structure polymorph in which both Fe and P occupy corner-shared tetrahedral as in SiO_2 quartz,[23] and $FePO_4$ glass has been formed by quenching from the melt.[24] Direct *ex situ* TEM observations, such as the image and corresponding electron diffraction pattern in Figure 10, indicate that the structure of charged particles is indeed highly disordered. We have not

(23) Mittal, R.; Chaplot, S. L.; Kolesnikov, A. I.; Loong, C.-K; Jayakumar, O. D.; Kulshreshtha, S. K. *Phys. Rev. B* **2002**, *66*, 174304.
(24) Friebele, E. J.; Wilson, L. K.; Dozier, A. K.; Kinser, D. L. *Phys. Status Solidi B* **1971**, *45*, 323.

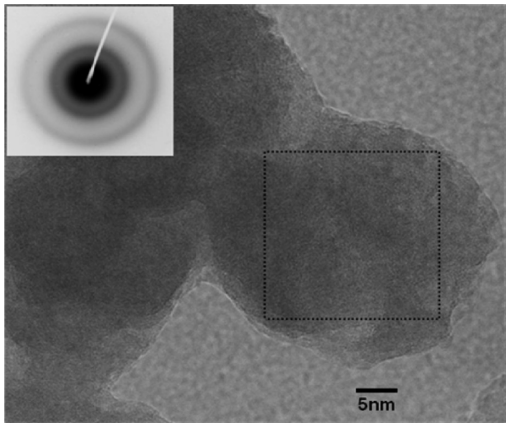

Figure 10. Amorphous phase particles observed in an electrode of Sample B charged galvanostatically to 100% SOC at C/5 rate and corresponding electron diffraction pattern.

determined detailed atomistic aspects in the amorphous structure. There may also be unexpected underpotential effects during discharge − the galvanostatic cycling data clearly shows that the amorphous phase can be retained upon relithiation. The details of this behavior remain to be understood. Together, the effects of particle size,[9] composition[3,10], and overpotential on phase stability and phase transformation pathways illustrate a richness of behavior in the olivines far beyond that of a "simple" first-order phase transition. Similar complexity of behavior may occur in orthosilicates such as Li_2FeSiO_4, and crystalline Si, which amorphizes during lithiation.[1,2] We suggest that phase transformation pathways in these materials may also be sensitive to overpotential.

Conclusions

The propensity toward amorphization of olivine cathodes during electrochemical cycling is shown to be a function of particle size and applied overpotential, in accordance with predictions from a phase-field model. The details of phase stability can be influenced by defect content and composition, and results may therefore be sample dependent. For the materials studied here, it is found that amorphization is maximized at intermediate levels of overpotential, with a crystal−crystal transformation being favored at both lower and higher overpotential values. Based on these results, several phase transformation pathways are expected to be available to olivines used under dynamic real-world cycling conditions.

Acknowledgment. This work was supported by DOE project number DE-SC0002626. Research at the National Synchrotron Light Source X14A beamline was partially sponsored by the U.S. Department of Energy, Office of Energy Efficiency and Renewable Energy, Vehicle Technologies Program, through the Oak Ridge National Laboratory's High Temperature Materials Laboratory User Program and by the Scientific User Facilities Division, Office of Basic Energy Sciences, U.S. Department of Energy. Y.-H.K. acknowledges support by Taiwan Merit Scholarship TMS-94-2A-019, M.T. acknowledges financial support from the Lawrence Postdoctoral Fellowship provided by the Lawrence Livermore National Laboratory, and N.M. acknowledges support by the Thailand Center of Excellence in Physics.